

## THz spectroscopy of VO<sub>2</sub> epitaxial films: controlling the anisotropic properties through strain engineering

This article has been downloaded from IOPscience. Please scroll down to see the full text article.

2012 New J. Phys. 14 083026

(<http://iopscience.iop.org/1367-2630/14/8/083026>)

View [the table of contents for this issue](#), or go to the [journal homepage](#) for more

Download details:

IP Address: 132.239.69.193

The article was downloaded on 30/08/2012 at 17:50

Please note that [terms and conditions apply](#).

## THz spectroscopy of VO<sub>2</sub> epitaxial films: controlling the anisotropic properties through strain engineering

Elsa Abreu<sup>1,4</sup>, Mengkun Liu<sup>1,4</sup>, Jiwei Lu<sup>2,4</sup>, Kevin G West<sup>2</sup>,  
Salinporn Kittiwatanakul<sup>3</sup>, Wenjing Yin<sup>2</sup>, Stuart A Wolf<sup>2,3</sup>  
and Richard D Averitt<sup>1,5</sup>

<sup>1</sup> Department of Physics, Boston University, Boston, MA 02215, USA

<sup>2</sup> Department of Materials Science and Engineering, University of Virginia, Charlottesville, VA 22904, USA

<sup>3</sup> Department of Physics, University of Virginia, Charlottesville, VA 22904, USA

E-mail: [raveritt@physics.bu.edu](mailto:raveritt@physics.bu.edu)

*New Journal of Physics* **14** (2012) 083026 (19pp)

Received 16 January 2012

Published 22 August 2012

Online at <http://www.njp.org/>

doi:10.1088/1367-2630/14/8/083026

**Abstract.** We use THz time-domain spectroscopy to investigate the far-infrared properties of vanadium dioxide thin films, strain-engineered through epitaxial growth on (100)<sub>R</sub> TiO<sub>2</sub> substrates. The films exhibit a large uniaxial tensile strain along the rutile *c*-axis. X-ray diffraction measurements reveal a structural transition temperature of 340 K, whereas independent THz conductivity measurements yield a metal–insulator transition temperature of 365 K along *c*<sub>R</sub>. Analysis of these results suggests a Mott–Hubbard behavior along the *c*<sub>R</sub>-axis. Along *c*<sub>R</sub> the conductivity is approximately 5500 (Ω cm)<sup>−1</sup>, comparable to bulk single crystals. The tensile strain leads to remarkably uniform cracking oriented along the rutile *c*-axis, resulting in a large conductivity anisotropy in our single-crystal epitaxial thin films. We discuss our results in the context of previous measurements and calculations of the properties of VO<sub>2</sub>, under different strain conditions. This work demonstrates the potential of strain engineering to tune the properties of complex materials while also serving as a powerful discriminatory tool for probing microscopic responses.

<sup>4</sup> These authors contributed equally to this work.

<sup>5</sup> Author to whom any correspondence should be addressed.

**Contents**

<b>1. Introduction</b>	<b>2</b>
<b>2. Experiments</b>	<b>3</b>
<b>3. Results</b>	<b>3</b>
3.1. Characterization of the VO <sub>2</sub> thin films . . . . .	3
3.2. THz time-domain spectroscopy . . . . .	5
<b>4. Discussion</b>	<b>9</b>
<b>5. Conclusion</b>	<b>15</b>
<b>Acknowledgments</b>	<b>15</b>
<b>References</b>	<b>16</b>

**1. Introduction**

Over the last five decades, vanadates have been intensively investigated with the aim of clarifying the physics of metal–insulator transitions (MIT). Vanadium dioxide (VO<sub>2</sub>) is particularly interesting, exhibiting an MIT with a conductivity decrease of over five orders of magnitude [1]. This is accompanied by a transition from a high-temperature metallic rutile structure to an insulating monoclinic structure below the transition temperature. In bulk, the structural transition temperature,  $T_{\text{St}}^{\text{bulk}}$ , equals the MIT temperature,  $T_{\text{MI}}^{\text{bulk}}$ , i.e.  $T_{\text{St}}^{\text{bulk}} \simeq T_{\text{MI}}^{\text{bulk}} \simeq 340$  K [2]. However, VO<sub>2</sub> is not yet fully understood regarding the Mott–Hubbard or Peierls-like nature of its MIT, although it is now generally accepted that a complete description requires the explicit consideration of electron–electron correlations [3, 4]. This is motivated, in particular, by the observed difference between the MIT and the structural transition temperatures, which gives significant evidence that the correlated conductivity behavior is independent of the structural phase [5–7]. Additionally, recent experimental studies highlight the multifunctional potential of VO<sub>2</sub> including current or photoinduced phase changes (with the commensurate large tuning of the dielectric function) as well as integration with other technologies for applications including light detection and memory-based metamaterials [8–10].

Strain engineering enables one to achieve an additional degree of control of technologically relevant properties and provides a discriminatory capability towards gaining fundamental insights into the microscopic origin of macroscopic characteristics. Strain has been used to modify the MIT temperature in VO<sub>2</sub> through direct application [11] or substrate-dependent application [12, 13] of stress. For the present measurements, we investigate highly strained epitaxial (100)<sub>R</sub> VO<sub>2</sub> thin films. The far-infrared conductivity is measured using non-contact polarization-sensitive terahertz time-domain spectroscopy (THz-TDS) providing direct access to the coherent quasiparticle response along  $b_{\text{R}}$  or  $c_{\text{R}}$  by simply changing the sample orientation. Previous investigations of VO<sub>2</sub> using THz spectroscopy [5, 10, 14–22] focused on the mechanism and dynamics of the MIT or on technological applications without, however, analyzing the anisotropic properties and the resultant impact on the temperature dependence of the structural and electronic transitions. Our analysis indicates that strain-engineered tuning of vanadium  $a_{1g}$  and  $e_g^{\pi}$  orbitals controls the MIT transition temperature along  $c_{\text{R}}$ , which is different from the structural transition temperature. The origin of the observed conductivity anisotropy is also discussed, along with the potential for a technological application of strain-engineered VO<sub>2</sub> thin films as temperature-switched far-infrared polarizers.

## 2. Experiments

The  $\sim 100$  and  $\sim 250$  nm thick  $\text{VO}_2$  films we investigated had been deposited on rutile  $(100)_R$   $\text{TiO}_2$  substrates by temperature-optimized sputtering from a vanadium target using the reactive bias target ion beam deposition technique in an  $\text{Ar} + \text{O}_2$  gas mixture; the details of the growth conditions can be found elsewhere [23]. The samples' morphology was characterized by optical microscopy, atomic force microscopy (AFM) and scanning electron microscopy (SEM), and the film microstructure was analyzed by temperature-dependent x-ray diffraction (XRD).

THz-TDS is a non-contact method for measuring far-infrared conductivity. The conductivity anisotropy is easily determined from the transmission of THz pulses for different sample orientations. In our case the output of a 1 kHz 35 fs Ti:sapphire amplifier is used to generate nearly single-cycle THz pulses via optical rectification in a ZnTe crystal. We then employ a standard THz-TDS setup to measure the transmission in the THz frequency range,  $\sim 0.2$ – $2.0$  THz [24]. By changing the sample orientation with respect to the THz pulse polarization, we are able to monitor the transmission along different crystal axes.

Frequency-domain transmission data are obtained by Fourier transforming the experimentally determined time-domain THz transmission of the film and that of a bare  $\text{TiO}_2$  substrate, used as the reference. The conductivity of the  $\text{VO}_2$  film is extracted from the ratio of the frequency-domain THz transmission of the film to the frequency-domain THz transmission of the reference, using appropriate Fresnel equations for a thin film on a substrate. THz-TDS provides an all-optical polarization-sensitive means of rapidly characterizing the conductivity anisotropy in many samples with different thicknesses and substrates.

## 3. Results

### 3.1. Characterization of the $\text{VO}_2$ thin films

Detailed room temperature XRD of the 100 nm thick  $\text{VO}_2$  film confirms the single-crystal nature of the sample and yields the lattice parameters of the material (figure 1(a)). Comparing these values with those in the rutile phase of bulk  $\text{VO}_2$  [25] yields strain values of  $-0.83\%$  along  $a_R$ ,  $-2.17\%$  along  $b_R$  and  $1.41\%$  along  $c_R$ , indicative of a compressive strain along  $a_R$  and  $b_R$ , as opposed to a tensile strain along  $c_R$ . Such strain values along  $c_R$  are comparable to those achieved in one-dimensional (1D)  $\text{VO}_2$  nanobeams [26]. Bulk rutile  $\text{TiO}_2$  has larger lattice constants than bulk rutile  $\text{VO}_2$  along all directions, so one would expect that both  $b_R$  and  $c_R$  would expand in  $(100)_R$   $\text{VO}_2$  films grown on a  $(100)_R$   $\text{TiO}_2$  substrate. However, our films show that the expansion along  $c_R$  surpasses the substrate clamping effect along the  $b_R$ -axis, leading to a compressive strain in the  $ab_R$ -plane. This behavior is also observed in the 250 nm thick film, with strain values of  $-0.68\%$  along  $a_R^{250\text{nm}}$ ,  $-1.94\%$  along  $b_R^{250\text{nm}}$  and  $0.86\%$  along  $c_R^{250\text{nm}}$ .

Temperature-dependent XRD results for the 100 nm thick film (figure 1(c)) show that a small  $a_R$ -axis expansion,  $\sim 0.1\%$ , occurs during the film's structural transition. This transition occurs at a temperature  $T_{\text{St}}^{\text{film}} \simeq 340 \text{ K} \simeq T_{\text{St}}^{\text{bulk}}$ , the same as in bulk, and shows the expected hysteretic behavior. (From here on,  $T_{\text{St}}$  will refer to both bulk and film structural transition temperatures.) The  $a_R$ -axis expansion in our strained sheet can be compared to that in bulk  $\text{VO}_2$ , estimated as  $\frac{a_R - b_M}{b} \simeq 0.6$ – $0.8\%$  [2, 27], where  $b_M$  is the equivalent of  $a_R$  in the bulk monoclinic insulating structure. The order of magnitude difference between the lattice parameter variation in the film and that in bulk stems from the clamping effect of the rutile  $\text{TiO}_2$  substrate. This

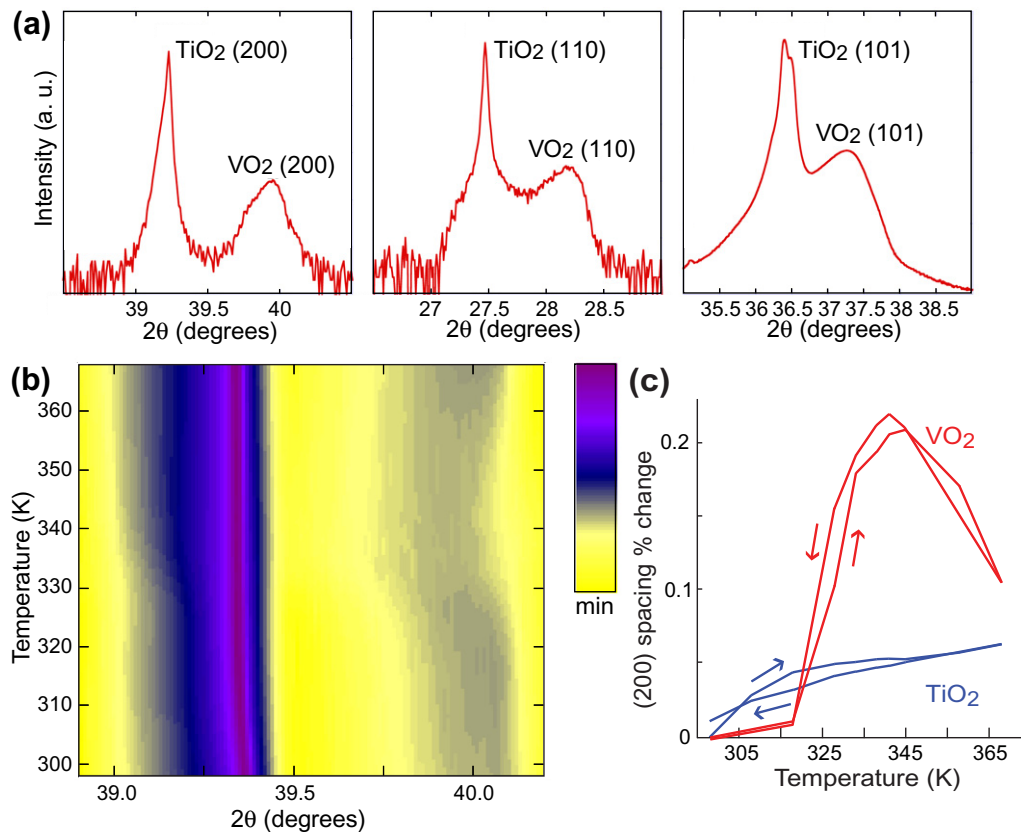


**Figure 1.** XRD characterization of the 100 nm VO<sub>2</sub> thin film. (a) Room-temperature XRD along three directions: (200)<sub>R</sub>, (110)<sub>R</sub> and (101)<sub>R</sub>. The lattice parameters can be estimated as 4.52 Å along  $a_R$ , 4.46 Å along  $b_R$  and 2.89 Å along  $c_R$ , yielding strain values of  $-0.83\%$  along  $a_R$ ,  $-2.17\%$  along  $b_R$  and  $1.41\%$  along  $c_R$ . (b) Temperature-dependent XRD. Both the TiO<sub>2</sub> and VO<sub>2</sub> (200)<sub>R</sub> peaks are seen to shift as a function of temperature. There is no evidence of the development of any additional structural phase. (c) Temperature dependence (for increasing and decreasing temperature) of the  $a_R$ -axis lattice spacing, deduced from the XRD data in (b): a  $\sim 0.1\%$  increase is observed along  $a_R$  across the structural transition which occurs at  $T_{St} \simeq 340$  K. The expected linear increase of the  $a_R$ -axis lattice spacing of TiO<sub>2</sub> with temperature is also observed.

is consistent with the large strain observed in room temperature XRD, caused by the strong substrate clamping effect. The structural change exhibited at 340 K by our strained VO<sub>2</sub> thin films is thus smaller than the change observed in bulk VO<sub>2</sub>. Since VO<sub>2</sub> shares the TiO<sub>2</sub> rutile structure at high temperatures, the reduced structural change is expected to have an impact mainly on the low-temperature VO<sub>2</sub> film's structure. The temperature-dependent (200)<sub>R</sub>  $2\theta$  plots from which the data in figure 1(c) were extracted are presented in figure 1(b). These raw data provide further support to our observation that the clamping effect due to the substrate is very strong, thereby preventing the development of significantly different structural phases in

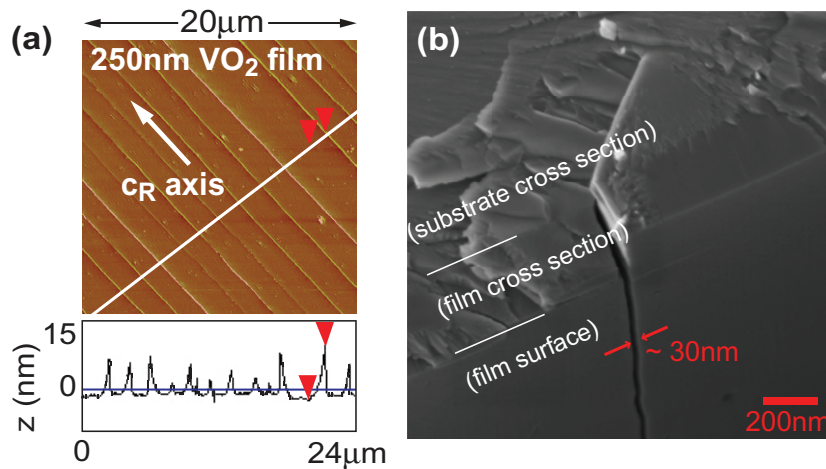


**Figure 2.** Characterization of the 250 nm thick  $(100)_R$   $\text{VO}_2$  film. (a) AFM phase image ( $0^\circ$ – $5^\circ$  scale) and corresponding height profile: the 250 nm sample shows buckling-induced ridges along  $c_R$  (height indicated by the arrows:  $\Delta z = 14.307$  nm). (b) SEM image of a section of the sample (seen from the edge, the surface and the cross section being located as labeled) showing a  $\sim 30$  nm wide crack.

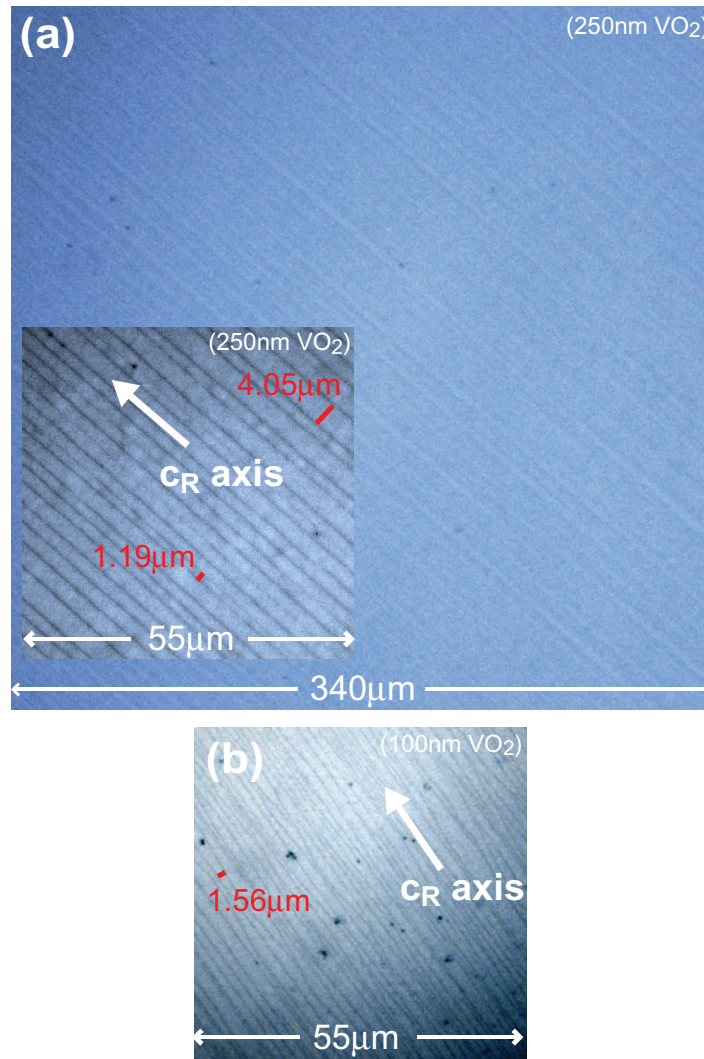
the strained  $\text{VO}_2$  film. The temperature-dependent XRD results for the 250 nm thick film are analogous to the results for the 100 nm thick film.

Figure 2(a) is an AFM phase image of the 250 nm film, showing periodic buckling and cracking of the film parallel to  $c_R$ , with inter-crack spacings of the order of  $1 \mu\text{m}$ . The depth profile reveals nanosized ridges,  $\sim 15$  nm high, near the cracks. The SEM image in figure 2(b) confirms the  $\sim 250$  nm thickness of the film. It shows that the cracks' depth matches the film thickness, and gives an estimate of about 30 nm for their width. These nanocracks were not detected by the AFM (figure 2(a)) due to lack of tip sensitivity.

The optical images of the 100 nm (figure 3(a)) and the 250 nm (figure 3(b)) films confirm the  $\sim 1 \mu\text{m}$  period spacing of the cracks along  $c_R$ . Also, the observed uniformity in the distribution of cracks is an indication that our films are strained in a highly homogeneous and oriented fashion. This crack distribution enables a comparison of our results with those of  $\text{VO}_2$  nanobeams, aligned along  $c_R$  [13, 26, 28–30], although the dimensionality of our films gives access to the properties of strained  $\text{VO}_2$  along more than one axis. Such cracking uniformity was achieved by optimizing the growth conditions of the samples, in particular the growth temperature. In the case of our  $(100)_R$   $\text{VO}_2$  films, the growth temperature was set to  $\sim 500^\circ\text{C}$ . Films grown at  $\sim 450^\circ\text{C}$  show cracking along different directions, which makes characterization of the films along  $c_R$  less straightforward. All subsequent analysis is analogous for both our 100 nm and 250 nm thick films, which exhibit cracks uniformly oriented along  $c_R$  (figure 3). Unless otherwise specified the results will refer to the 100 nm thick sample.

### 3.2. THz time-domain spectroscopy

$(100)_R$   $\text{TiO}_2$  has a large refractive index anisotropy in the THz range, partly caused by its characteristic rutile structure. Such an anisotropy in the  $(100)_R$   $\text{TiO}_2$  substrate makes it easy



**Figure 3.** Characterization of VO<sub>2</sub> thin films on a (100)<sub>R</sub> TiO<sub>2</sub> substrate. Optical images of the (a) 250 nm and (b) 100 nm films: the samples show buckling-induced ridges along  $c_R$ , spaced by  $\sim 1 \mu\text{m}$ .

to distinguish the transmitted THz signals with polarization parallel to  $c_R$  from the THz signals with polarization perpendicular to  $b_R$  (figure 4). Temperature-dependent experimental characterization of the TiO<sub>2</sub> substrate in the THz range, using our THz-TDS setup, led to values of

$$n_e \simeq 12.4 - 6 \times 10^{-4} \Delta T + 1.2i,$$

$$n_o \simeq 9.1 - 3 \times 10^{-4} \Delta T + 0.4i,$$

for the refractive index along  $c_R$  and  $b_R$ , respectively, in agreement with previous results [31]. Here,  $\Delta T$  stands for the temperature deviation with respect to room temperature. This approximation to the TiO<sub>2</sub> complex refractive index holds between room temperature and 400 K; it does not take into account the temperature dependence of the imaginary part, which is negligible for our purposes.

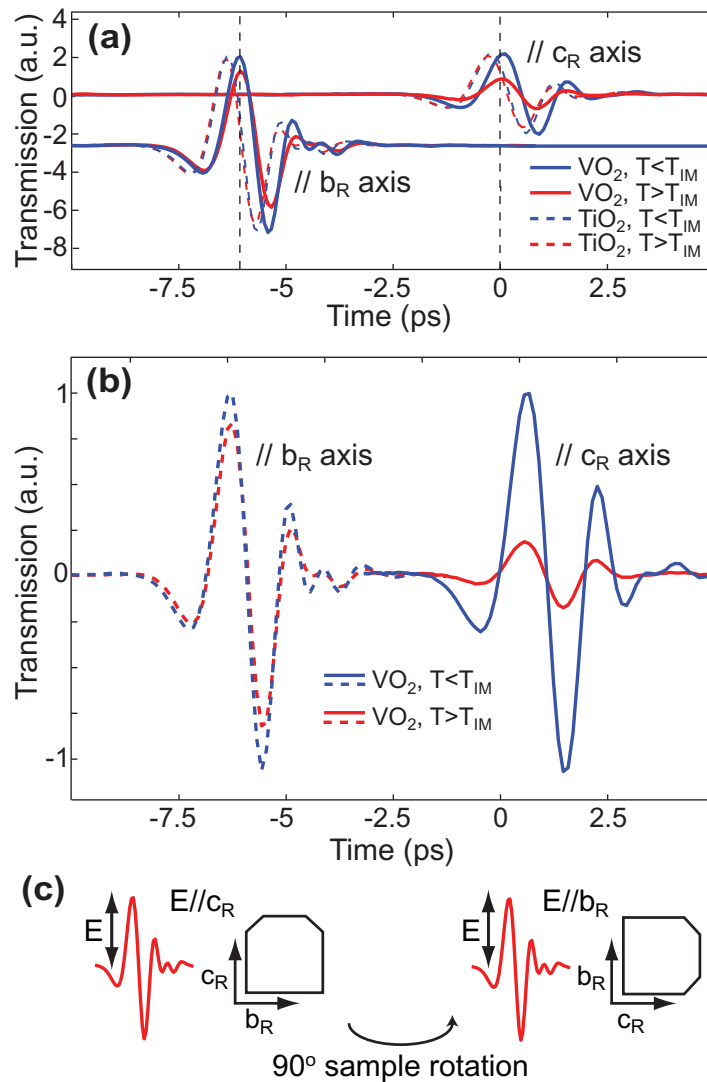


**Figure 4.** (a) THz transmission along  $c_R$  and  $b_R$  (vertically offset) in the 100 nm (100)<sub>R</sub> VO<sub>2</sub> sample (solid) and in the TiO<sub>2</sub> reference substrate (dashed), below (blue) and above (red)  $T_{MI}$ . The large refractive index anisotropy of the TiO<sub>2</sub> substrate leads to a slower propagation of the laser pulse along  $c_R$  than along  $b_R$ , which enables the distinction of the two signals in time and thus the orientation of the sample with respect to the incident field polarization. (b) THz transmission along  $c_R$  and  $b_R$  in the 250 nm (100)<sub>R</sub> VO<sub>2</sub> sample, below (blue) and above (red)  $T_{MI}$ , normalized to the low temperature value. The relative high-temperature transmission along  $b_R$  ( $\sim 85\%$ ) is dramatically different from that along  $c_R$  ( $\sim 15\%$ ). (c) The  $c_R$ -axis ( $b_R$ -axis) of the films is oriented parallel to the THz field polarization in order to measure the transmission along  $c_R$  ( $b_R$ ).

As shown in figure 4, upon increasing the temperature from the insulating to the metallic phase the THz peak transmission in the 100 nm (100)<sub>R</sub> VO<sub>2</sub> film decreases by  $\sim 70\%$  along the  $c_R$ -axis and by  $\sim 15\%$  along the  $b_R$ -axis, and the THz peak transmission in the 250 nm (100)<sub>R</sub>

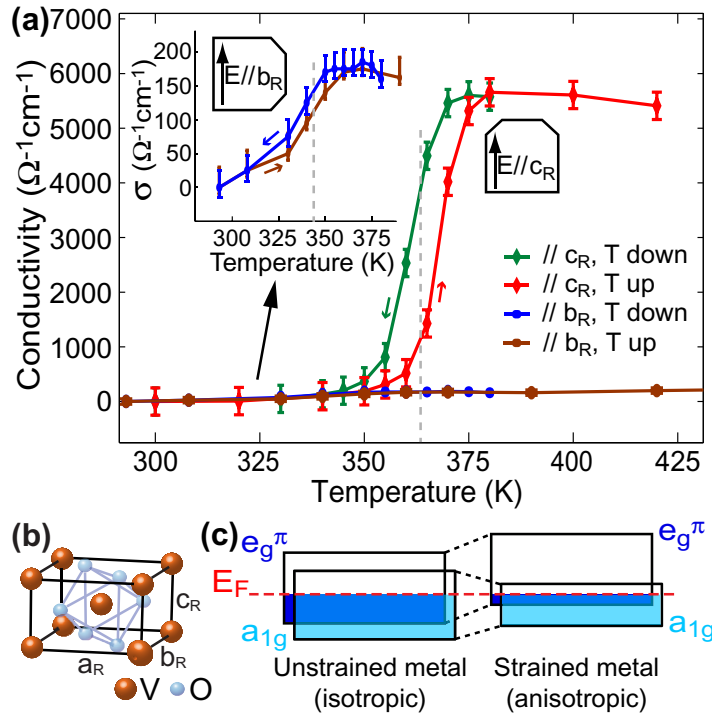


**Figure 5.** (a) Temperature dependence of the far-IR conductivity in 100 nm  $(100)_R \text{VO}_2$ :  $\sigma_{c_R} \simeq 30\sigma_{b_R}$  above the MIT temperature;  $T_{\text{MI}}^{c_R} \simeq 365$  K while  $T_{\text{MI}}^{b_R} \simeq 340$  K  $\simeq T_{\text{MI}}^{\text{bulk}}$ . The insets show the laser polarization direction with respect to the  $\text{VO}_2$  sample: the polarization is oriented parallel to the  $c_R$ -axis ( $b_R$ -axis) in order to measure the transmission, and determine the conductivity, along  $c_R$  ( $b_R$ ). (b) The  $\text{VO}_2$  rutile unit cell, following Eyert [33]. (c) Effect of tensile strain along  $c_R$  on the electronic structure of metallic  $\text{VO}_2$ : antibonding  $e_g^\pi$  bands are shifted upwards while the  $a_{1g}$  band is narrowed.

$\text{VO}_2$  film decreases by  $\sim 85\%$  along the  $c_R$ -axis and by  $\sim 15\%$  along the  $b_R$ -axis. Figure 4(b) shows the time-domain transmission anisotropy in our 250 nm  $\text{VO}_2$  sample, transmission data being normalized to their low-temperature value along each axis ( $b_R$  and  $c_R$ ).

Figure 5(a) shows the temperature-dependent far-infrared conductivity for the 100 nm  $(100)_R \text{VO}_2$  thin film, obtained from the transmission data as detailed above. The conductivity along  $c_R$  shows a clear transition from the insulating to the metallic state with a narrow hysteresis, which is indicative of the high quality of the sample. In the metallic state the conductivity is  $\sigma_{c_R} \simeq 5650$  ( $\Omega \text{cm}$ ) $^{-1}$ , comparable to bulk single-crystal values [1]. The MIT along  $c_R$  occurs at a temperature  $T_{\text{MI}}^{c_R} \simeq 365$  K.  $T_{\text{MI}}^{c_R}$  is significantly larger than both the structural transition temperature and the bulk MIT temperature,  $T_{\text{St}} \simeq T_{\text{MI}}^{\text{bulk}} \simeq 340$  K. Our  $\text{VO}_2$  film therefore exhibits, along  $c_R$ , a  $\sim 25$  K temperature difference between the structural and the MIT temperatures. The combination of the quasi-three dimensionality of our films, which enables a direct measurement of the strain along the three crystal axes through XRD analysis, with the polarization sensitivity of THz spectroscopy is key to identifying this distinction between the two transition temperatures.

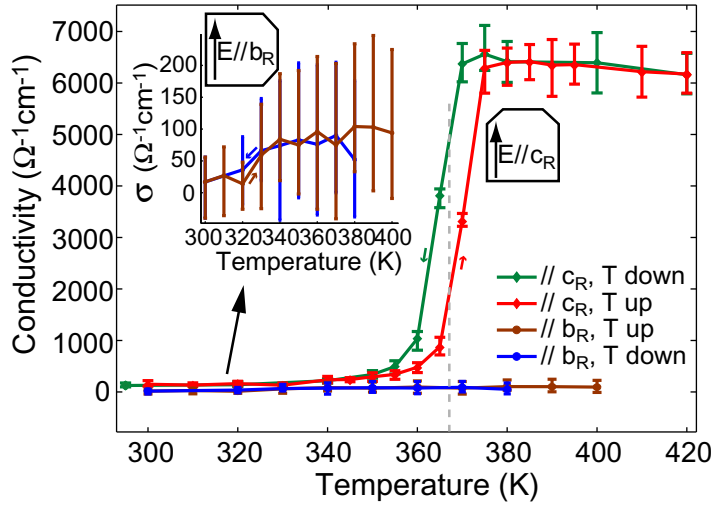


**Figure 6.** Temperature dependence of the far-IR conductivity in 250 nm  $(100)_R$   $\text{VO}_2$ :  $\sigma_{c_R} \simeq 6250 (\Omega \text{ cm})^{-1}$  for  $T > T_{\text{MI}}^{c_R} \simeq 365 \text{ K}$ ;  $\sigma_{b_R} < 100 (\Omega \text{ cm})^{-1}$  and  $T_{\text{MI}}^{b_R}$  can only be estimated as  $T_{\text{MI}}^{b_R} \simeq 340 \text{ K}$ . The insets show the laser polarization direction with respect to the  $\text{VO}_2$  sample: the polarization is oriented parallel to the  $c_R$ -axis ( $b_R$ -axis) in order to measure the transmission, and determine the conductivity, along  $c_R$  ( $b_R$ ).

The conductivity along  $b_R$  also exhibits a transition (see the inset of figure 5(a)), which occurs at  $T_{\text{MI}}^{b_R} \simeq 340 \text{ K}$ . Along this direction we therefore observe that the structural and MIT temperatures are the same,  $T_{\text{MI}}^{b_R} \simeq T_{\text{St}} \simeq T_{\text{MI}}^{\text{bulk}}$ . However, the conductivity along  $b_R$  reaches a high-temperature value about 30 times smaller than the high-temperature conductivity along  $c_R$ . This strong conductivity anisotropy will be addressed later in the text.

THz-TDS results for the 250 nm thick sample (figure 6) indicate that its transport properties are similar to those of the 100 nm sample. In particular, the high-temperature conductivity along  $c_R$  remains as good as that in bulk  $\text{VO}_2$  single crystals [1] when  $T_{\text{MI}}^{c_R} \simeq 365 \text{ K} > T_{\text{St}}$ . The high-temperature conductivity along  $b_R$  is very low,  $< 100 (\Omega \text{ cm})^{-1}$ , and the MIT temperature can only be estimated at  $T_{\text{MI}}^{b_R} \simeq 340 \text{ K}$ , consistent with  $T_{\text{MI}}^{\text{bulk}}$  and  $T_{\text{St}}$  and in line with what is observed in the 100 nm sample (figure 5(a)).

#### 4. Discussion

Understanding the contribution of the V3d orbitals to the electronic properties is crucial to explain the large material anisotropy in  $T_{\text{MI}}$  [32]. A splitting of the fivefold degenerate 3d states occurs due to the octahedral coordination of the V atoms (figure 5(b)), resulting in a higher-energy doubly degenerate  $e_g$  level and a lower-energy triply degenerate  $t_{2g}$  level. Trigonal distortion further splits the  $t_{2g}$  levels, leading to an upshifted doubly degenerate  $e_g^\pi$  state, responsible for conduction in the  $ab_R$ -plane, while downshifting a non-degenerate  $c_R$ -oriented  $a_{1g}$  state. Recent cluster dynamical mean field theory (cDMFT) calculations [4], which include the effect of a  $\pm 2\%$  strain along  $c_R$ , have demonstrated that a tensile strain along  $c_R$  narrows the  $a_{1g}$ -derived band and leads to a compressive strain in the  $ab_R$ -plane, which uplifts the  $e_g^\pi$  band (figure 5(c)). In the Mott picture the energy increase of  $e_g^\pi$  electrons reduces

the screening of electrons residing in the  $a_{1g}$  band, thereby enhancing the effect of correlations (i.e. increasing the screened Hubbard  $U$ ). This results in an increase of the insulating band gap that opens, below  $T_{\text{MI}}$ , between the bonding  $a_{1g}$  and the anti-bonding  $e_g^\pi$  levels, therefore leading to an increased  $T_{\text{MI}}$  along  $c_{\text{R}}$  [33, 34].

The epitaxial strain in our film can be decomposed into a uniaxial tensile strain along  $c_{\text{R}}$  and a uniaxial compressive strain along  $b_{\text{R}}$ . Along  $c_{\text{R}}$ ,  $T_{\text{MI}}^{\text{cR}} \simeq 365 \text{ K} > T_{\text{MI}}^{\text{bulk}}$ , in line with previous experimental results [11], while  $\sigma_{c_{\text{R}}}$  remains comparable to the best bulk single crystal values [1]. These results agree with the Mott picture above, where the increased lattice spacing along  $c_{\text{R}}$  further increases the ratio of Coulomb repulsion to the inter-atomic hopping integral, thereby destabilizing the metallic phase and increasing  $T_{\text{MI}}^{\text{cR}}$ . The Peierls picture predicts a decrease in  $T_{\text{MI}}^{\text{cR}}$  with tensile strain along  $c_{\text{R}}$ , associated with a stabilization of the metallic state where vanadium atoms are unpaired, thus failing to describe our results along that axis [4]. Also contrary to the Peierls-driven MIT scenario along  $c_{\text{R}}$  is the fact that the structural transition occurs at a temperature  $T_{\text{St}} \simeq 340$ ,  $\sim 25 \text{ K}$  lower than  $T_{\text{MI}}^{\text{cR}}$ : in a Peierls picture the MIT is driven by the structural transition so that both transitions would be expected to occur at the same temperature. In contrast to what happens along  $c_{\text{R}}$ , the results along  $b_{\text{R}}$ , where  $T_{\text{MI}}^{b_{\text{R}}} \simeq T_{\text{St}}$ , are compatible with a Peierls-driven MIT scenario.

As mentioned above, our samples are cracked along  $c_{\text{R}}$ . The occurrence of such cracks is common in  $\text{VO}_2$ , in both bulk and strained samples [35, 36], and it has prevented accurate measurements of the dc conductivity in this material in the direction perpendicular to  $c_{\text{R}}$ . Hindered quasiparticle motion along  $b_{\text{R}}$  due to the presence of  $c_{\text{R}}$ -oriented cracks is the most likely explanation for the reduced value of  $\sigma_{b_{\text{R}}}$  in our films. However, a different scenario could arise in the THz range. Due to the small value of the far-infrared carrier mean free path (of the order of  $\text{\AA}$  [37]) compared to dc, the  $\sim 1 \text{ ps}$  long THz field should be able to couple to the material along  $b_{\text{R}}$  despite the cracks along  $c_{\text{R}}$ . According to this picture, the uniaxial compressive strain along  $b_{\text{R}}$  would play a significant role in reducing  $\sigma_{b_{\text{R}}}$ , compared to  $\sigma_{c_{\text{R}}}$ , while keeping  $T_{\text{MI}}^{b_{\text{R}}} \simeq T_{\text{MI}}^{\text{bulk}} \simeq T_{\text{St}}$ . Given the orbitals' orientation, conductivity in the  $ab_{\text{R}}$ -plane is mediated by the  $e_g^\pi$  orbitals whose energy is controlled by the overlap between  $\text{O}2p$  and  $\text{V}3d$  orbitals [33]. Low-conductivity behavior in the compressed  $ab_{\text{R}}$ -plane for  $T > T_{\text{MI}}$  would then arise from the  $e_g^\pi$  states being higher in energy than in the unstrained case, which reduces their overlap with the Fermi level (figure 5(c)).  $\text{VO}_2$  thin films that remain uncracked while maintaining a high level of strain along  $b_{\text{R}}$  must be investigated in order to clarify the effect of the  $e_g^\pi$  orbitals on the high-temperature value of  $\sigma_{b_{\text{R}}}$ , thereby also clarifying the nature of the MIT along this axis.

Our strained  $\text{VO}_2$  films on a  $\text{TiO}_2$  substrate have been shown to enable the separation of the far-infrared signal's polarization components in both time and intensity (figure 4). The temperature-dependent THz conductivity of strained  $\text{VO}_2$  thin films (figures 5(a) and 6) shows that incident light polarized parallel to  $b_{\text{R}}$  is transmitted through  $\text{VO}_2$  at both low and high temperatures, whereas incident light polarized parallel to  $c_{\text{R}}$  is transmitted through  $\text{VO}_2$  at low temperatures but reflected at high temperatures. Our strained  $\text{VO}_2$  single-crystal films can thus be thought of as temperature-switchable far-infrared polarizing beam-splitters.

Finally, it is interesting to map the strain of our film onto the  $\text{VO}_2$  phase diagram in figure 7, constructed based on past studies of  $\text{VO}_2$  as a function of temperature, pressure [26, 38] and doping [39–42]. In general, it is not trivial to map the effect of doping onto that of pressure. This was initiated by Pouget *et al* [38, 41], who found a one-to-one correspondence between Cr doping and the application of uniaxial stress along  $[110]_{\text{R}}$ . Other doping experiments tend

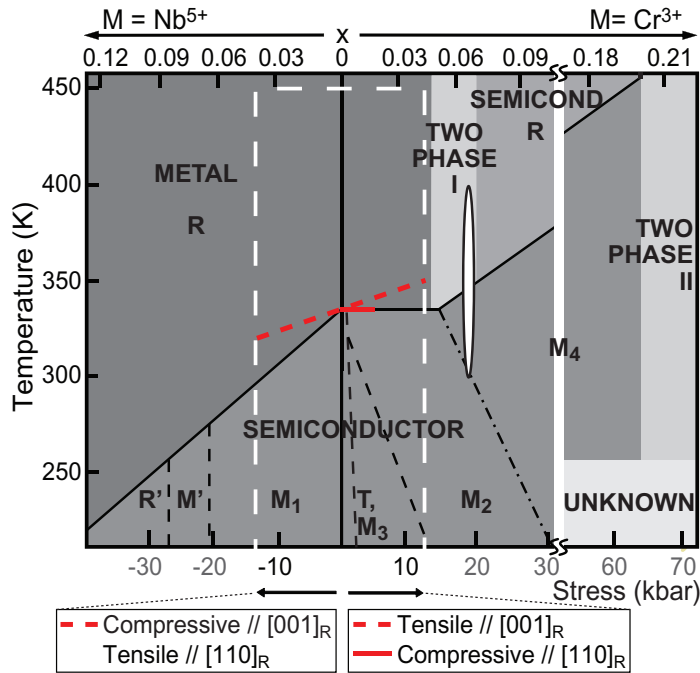


**Figure 7.** Phase diagram of  $\text{VO}_2$  for stress applied mostly along  $[110]_R$ . The black solid line indicates  $T_{\text{MI}}$ ; the white oval defines the phase space of our samples; uniaxial stress results are presented in the region delimited by the dashed white lines; doping ( $\text{V}_{1-x}\text{M}_x\text{O}_2$ ) leading to reduction ( $\text{M} = \text{Nb}^{5+}$ ) or oxidation ( $\text{M} = \text{Cr}^{3+}$ ) of  $\text{V}^{4+}$  is specified on the top horizontal axis [26, 38–42] (refer to the main text for more details).

to indicate that doping ions with radii smaller than  $\text{V}^{4+}$  leads to an increase in  $T_{\text{MI}}$ , whereas those with larger radii have the opposite effect [43]. This is similar to what happens in  $\text{V}_2\text{O}_3$ , a canonical Mott insulator [44].

Figure 7 compiles previous experimental results obtained on  $\text{VO}_2$  under different pressure [26, 38] and doping [39–42] conditions.  $P = 0$  corresponds to atmospheric pressure. The application of hydrostatic pressure [1, 45, 46] cannot be easily interpreted in terms of its influence on the conductivity or on  $T_{\text{MI}}$  along the individual axes of the crystalline structure; which is the main focus of our study. Therefore we do not include hydrostatic pressure data in the phase diagram of figure 7. The dashed white lines delimit the region of the phase diagram where uniaxial pressure was applied along  $[001]_R$  (up to 12 kbar), for both compression ( $P < 0$ ) and tension ( $P > 0$ ), and along  $[110]_R$  (up to 1.2 kbar) for compression alone ( $P > 0$ ). Within the rectangle, the dashed red line indicates  $T_{\text{MI}}^{\text{CR}}$  versus stress along  $c_R$ ,  $[001]_R$ , while the solid red line indicates  $T_{\text{MI}}^{\text{CR}}$  versus stress in the  $ab_R$ -plane,  $[110]_R$ . The dashed black lines separate different insulating phases within the low-temperature monoclinic phase. The dash-dotted line between phases  $M_2$  and  $M_4$  is a conjecture [39, 42]. Note that apart from the dashed red line, relative to stress along  $[001]_R$ , all of the information in the diagram refers to stress along  $[110]_R$ . The white oval indicates the phase space characteristic of our  $(100)_R$   $\text{VO}_2$  samples. The uniaxial stress on our films along  $[110]_R$  has been estimated for 100 and 250 nm samples to be  $\sim 20.9$  and  $\sim 18.5$  kbar, respectively, based on the measured  $-2.32$  and  $-2.06\%$  strain along  $(110)_R$

and on a Young modulus of 900 kbar [47]. These stress values are higher than ever reported, to our knowledge, for uniaxial stress on VO<sub>2</sub>.

The dependence of  $T_{\text{MI}}$  on doping, studied in  $V_{1-x}M_xO_2$  compounds, can be approximately mapped onto its dependence on applied pressure. Reduction of V<sup>4+</sup> is achieved using M = Nb, Mo, W, Ta, Re, Ir, F, Ti, Os, Ru, Tc and so on, with formal charges of +4, +5 or +6 [32, 43, 48–59]. The effect on  $T_{\text{MI}}$  is similar to that of negative (compressive) stress along [001]<sub>R</sub>, yielding  $dT_{\text{MI}}/dx = -0.3$  to  $-28$  K (at.% M)<sup>-1</sup>. Oxidation of V<sup>4+</sup> is achieved using M = Cr, Al, Fe, Ga, Ge, Sn, Mn, Co and so on, with formal charges of +3 or +4 [32, 40–43, 48, 60–65]. The effect on  $T_{\text{MI}}$  is similar to that of positive (tensile) stress along [001]<sub>R</sub>, yielding  $dT_{\text{MI}}/dx = 0$ –13 K (at.% M)<sup>-1</sup>.

Our results, indicated by the white oval in the phase diagram of figure 7, are comparable to those of Everhart *et al*, where an anisotropy of about two orders of magnitude is observed in the metallic phase of bulk VO<sub>2</sub> single crystals doped with iron at 0.076% [66]. Our estimate of the stress puts our samples in a region of the phase diagram where  $T_{\text{MI}}$  increases with stress and where two-phase behavior is expected above  $T_{\text{MI}}$ . This is consistent with our observation of both insulating ( $T < T_{\text{MI}}^{\text{CR}}$ ) and metallic ( $T > T_{\text{MI}}^{\text{CR}}$ ) values of  $\sigma_{c_R}$  in the same rutile structure, above  $T_{\text{St}}$ . The independence of the conductivity behavior from the structural phase has been reported earlier [5–7], though relative to monoclinic structures. As to the low-temperature structure, M4 and rutile seem to be the most likely candidates, although we cannot distinguish between the two. M1, M2 and M3/T are all structurally too far from rutile [30, 39, 40] to lead to the results shown in figure 1(c), and are located in different regions of the phase diagram, as seen in figure 7. These observations, along with the strong conductivity anisotropy exhibited by our strained thin films, are indicative of more complex behavior of VO<sub>2</sub>, beyond the currently accepted doping and strain dependence of its structural and transport properties (figure 7).

Coming back to the conductivity measured in our strained thin films, it is important to point out that its anisotropy is unexpectedly large compared to previous experimental observations and theoretical calculations on VO<sub>2</sub> samples [12, 61, 66–73, 81]. The anisotropy in dc conductivity,  $\frac{\sigma_{c_R}}{\sigma_{b_R}}$  or  $\frac{\sigma_{c_R}}{\sigma_{a_R}}$ , in undoped VO<sub>2</sub> samples is generally >1 for  $T < T_{\text{MI}}$  but can take many different values for  $T > T_{\text{MI}}$  (table 1). Differences in sample quality and stoichiometry as well as in conductivity measurement techniques surely affect the results, but variations in geometry and internal strain/cracking are also likely to have an effect on the anisotropy of metallic VO<sub>2</sub>.

Tables 1 and 2 present a complete and up-to-date review, to our knowledge, of the experimental and theoretical data on conductivity anisotropy in VO<sub>2</sub>, including the effect of externally applied stress. Table 1 includes the results on the conductivity anisotropy, above and below  $T_{\text{MI}}$ , when no external stress is applied [12, 61, 66–73]. Table 2 presents several results on the strain-induced variation of  $T_{\text{MI}}$  and of the conductivity in VO<sub>2</sub>, for situations where hydrostatic or uniaxial pressure is applied to the samples [1, 7, 11, 12, 26, 38, 45, 46, 74–76].

As seen in tables 1 and 2, in most situations where uniaxial pressure is applied, the conductivity is measured along  $c_R$ , the only axis along which it is well defined due to geometry constraints of the samples or to cracking. Few studies determine the conductivity along  $a_R$  or  $b_R$  as a function of applied pressure. In general, it is agreed that (i) an applied uniaxial compressive (tensile) stress along the  $c_R$ -axis leads to an increased (decreased) conductivity for  $T > T_{\text{MI}}$ ; (ii) an applied uniaxial tensile (compressive) stress along the  $c_R$ -axis leads to an increased (decreased)  $T_{\text{MI}}$  (the axis along which  $T_{\text{MI}}$  is measured is not always specified); (iii) a small uniaxial stress applied along the [110]<sub>R</sub> direction has no significant effect on the conductivity or on  $T_{\text{MI}}$  along  $c_R$ , but it promotes a phase transition between different monoclinic structures

**Table 1.** Compilation of previous experimental and theoretical results for the conductivity (dc, unless otherwise specified) anisotropy,  $\frac{\sigma_{c_R}}{\sigma_{b_R}}$  or  $\frac{\sigma_{c_R}}{\sigma_{a_R}}$ , in VO<sub>2</sub>, above and below  $T_{MI}$ , when no external stress is applied [12, 61, 66–73].

Publication	Sample type	Method	Anisotropy below $T_{MI}$	Anisotropy above $T_{MI}$
Bongers [68]	Bulk single crystal (needle along $c_R$ , $6 \times 0.3 \times 0.15$ mm)	Two-probe	2	2.5
Barker [67]	Bulk polycrystal (well defined $c_R$ )	Hall voltage	0.7–0.8	1.1–2
Kosuge [61]	Bulk single crystal	Two-probe	1.14	0.58
Koide <i>et al</i> [81]	Single crystal film on rutile substrate	Two-probe	2	0.001–0.1
	Bulk single crystal (needle along $c_R$ , $3 \times 0.8 \times 0.07$ mm)	Two-probe	<1.2	0.33
Everhart [66]	Bulk single crystal ( $4-7 \times 1-4 \times 1-4$ mm)	Four-probe	2–10	7.5
Verleur [69]	Bulk single crystal	Reflectivity (0.25–5 eV)	0.28 – 1.4	0.79 – 2
Continenza [70]	(Calculations)	Model GW (0–10 eV)	3–6.7	N/A
Mossanek and Abbate [71]	(Calculations)	LDA (0–12 eV)	0.6–>3	0.7–3.3
Lysenko [72]	30 nm film on (012) Al <sub>2</sub> O <sub>3</sub>	Optical (400 nm) diffraction	1.05	1
Lu [12]	40 nm film on (011) <sub>R</sub> TiO <sub>2</sub>	Star-shaped electrodes	5.14	1
Tomczak [73]	(Calculations)	LDA+CDMFT (0–5 eV)	0.73–1.67	0.96–1.14
Our results	100 nm film on (100) <sub>R</sub> TiO <sub>2</sub>	THz-TDS (far IR)	N/A	~30

(M1, M2, T/M3 and M4), in the insulating phase [38–40]. Further experiments are needed in order to systematically measure the conductivity along  $a_R$  or  $b_R$  under (i) an applied uniaxial stress along  $a_R$  or  $b_R$ ; (ii) an applied uniaxial stress along  $c_R$ ; and (iii) hydrostatic pressure. Also, clear criteria for distinguishing  $T_{MI}$  from  $T_{SI}$  would be extremely valuable to help draw a more accurate and complete phase diagram, in line with what has been attempted in previous studies [5–7]. The highly oriented strain across a quasi-3D structure, achieved in epitaxially grown VO<sub>2</sub> thin films, gives them extraordinary versatility and potential in the investigation of these issues.

Theoretically, several pictures have been suggested to explain the anisotropy in (unstrained) VO<sub>2</sub>: (i) a two-band model description of 3d electrons, within the framework of the Goodenough model, predicts a non-conducting  $ab_R$ -plane for  $T > T_{MI}$ , any residual conductivity in that plane

**Table 2.** Compilation of previous experimental and theoretical results for the variation of  $T_{\text{MI}}$  and of the conductivity (dc, unless otherwise specified) in  $\text{VO}_2$ , under applied hydrostatic or uniaxial pressure. We assume that  $\Delta P > 0$  for compression and  $\Delta P < 0$  for expansion [1, 7, 11, 12, 26, 38, 45, 46, 74–76].

Publication	Sample type	Applied pressure	Conductivity versus pressure	Conductivity along ...	$dT_{\text{MI}}/dP$ (K kbar <sup>-1</sup> )	$dT_{\text{MI}}/dP$ along ...
Minomura and Hagasaki [74]	Uniaxial	Not specified (Drickamer cell, up to 160 kbar)	Not specified	–0.46	Not specified	
Neuman <i>et al</i> [45]	Single crystal	Hydrostatic (up to 6 kbar)	Increases below $T_{\text{MI}}$	Not specified	No significant change	Not specified
	Powder	Hydrostatic (up to 6 kbar)	Increases	Not specified	No significant change	Not specified
Berglund and Jayaraman [46]	Bulk single crystal (0.25 × 0.25 × 0.2 in, crack along $c_{\text{R}}$ )	Hydrostatic (up to 44 kbar)	Increases; saturates above $T_{\text{MI}}$ , at 15–20 kbar	$c_{\text{R}}$	0.082	$c_{\text{R}}$
Ladd and Paul [1]	Bulk single crystal (10 × 1 × 1 mm)	Hydrostatic (up to 8 kbar)	Increases (up to 30 kbar, at $T_{\text{room}}$ )	$c_{\text{R}}$	0.06	$c_{\text{R}}$
		Along $a_{\text{R}}$ or $b_{\text{R}}$	N/A	$c_{\text{R}}$	No significant change	$c_{\text{R}}$
		Along $c_{\text{R}}$ (up to 0.5 kbar)	Increases below $T_{\text{MI}}$	$c_{\text{R}}$	–1.2	$c_{\text{R}}$
Pouget <i>et al</i> [38]	Bulk single crystal (0.5 mm <sup>2</sup> × 2 mm, 3 mm <sup>2</sup> × 4 mm)	Along [110] <sub>R</sub> (up to 1.2 kbar)	No significant change	$c_{\text{R}}$	No significant change	$c_{\text{R}}$
Gregg and Bowman [75]	Thin films on Al <sub>2</sub> O <sub>3</sub> (012)	In-plane (three-point bend)	Increases below $T_{\text{MI}}$	Not specified	N/A	N/A
Muraoka <i>et al</i> [11]	10–15 nm thick single crystal thin films on (001) <sub>R</sub> and (110) <sub>R</sub> TiO <sub>2</sub>	Along $c_{\text{R}}$ (epitaxial: –0.3% for (001) <sub>R</sub> , 1.2% for (110) <sub>R</sub> )	Increases	$a_{\text{R}}$ or $b_{\text{R}}$ for [001] <sub>R</sub> ; not specified for [110] <sub>R</sub>	< 0	$a_{\text{R}}$ or $b_{\text{R}}$ for [001] <sub>R</sub> ; not specified for [110] <sub>R</sub>
Arcangeletti <i>et al</i> [7]	Single crystal (5 μm thick slab)	Uniaxial (diamond a. c., up to 140kbar)	Increases below $T_{\text{MI}}$ (750–6000 cm <sup>-1</sup> )	Not specified	N/A	N/A
Lu <i>et al</i> [12]	Single crystal thin film on (011) <sub>R</sub> TiO <sub>2</sub>	In-plane (epitaxial: –1.2%//[011] <sub>R</sub> , –0.4%//[001] <sub>R</sub> )	N/A	$a_{\text{R}}$ or $b_{\text{R}}$	< 0	$a_{\text{R}}$ or $b_{\text{R}}$
Sakai [76]	Polycrystalline thin film on metallic Ti ( $a_{\text{R}}$ in plane)	In-plane (point contact, up to 255kbar)	Increases	Not specified	> 0	Not specified
Cao <i>et al</i> [26]	Single crystal (0.5–2 × 0.5–2 × 100 nm, along $c_{\text{R}}$ )	Along $c_{\text{R}}$ (three-point bend, up to 12 kbar)	Increases (optical)	$c_{\text{R}}$	~–2	$c_{\text{R}}$
Our results	Single crystal thin film on (100) <sub>R</sub> TiO <sub>2</sub>	In-plane (epitaxial: 5.4%//[001] <sub>R</sub> , –2.3%//[010] <sub>R</sub> )	No significant change (far IR))	$c_{\text{R}}$	< 0	$c_{\text{R}}$
			Decreases above $T_{\text{MI}}$ (far IR)	$b_{\text{R}}$	No significant change	$b_{\text{R}}$

being due to the overlap of O2p and V3d orbitals [32, 33]; (ii) local density approximation (LDA) calculations by Allen's group predict the structural distortion to be the main force driving the MIT in VO<sub>2</sub>, following a simple Peierls picture [77]; (iii) a three-band Hubbard model, suggested by Tanaka *et al* [78], predicts a 1D conducting phase along  $c_R$  for  $T < T_{MI}$  and an isotropically conducting phase for  $T > T_{MI}$ ; (iv) LDA + cDMFT calculations by Biermann *et al* [3] suggest that electron correlations within the  $e_g^\pi$  levels are weaker than those along the  $a_{1g}$  ones; (v) subsequent LDA+cDMFT calculations by Kotliar's group, which include a moderate degree of uniaxial strain, suggest that electronic correlations are the main driving force in the MIT and that the rutile phase itself should be able to support both metallic and insulating electronic behavior [4]; (vi) Liebsch *et al* [79] compared the LDA+U, DMFT and GW approximation and found that none of them provides a full description of VO<sub>2</sub>, namely of the development of the insulating gap below  $T_{MI}$ . Nonetheless, most of the calculations based on unstrained VO<sub>2</sub> samples agree that (i)  $a_{1g}$  and  $e_g^\pi$  states can be regarded as nearly independent; (ii) the conductivity is expected to be of predominantly  $a_{1g}$  behavior for  $T < T_{MI}$  and nearly isotropic for  $T > T_{MI}$ ; (iii) electron correlations should be included in the model, mainly in the  $c_R$ -oriented  $a_{1g}$  levels. Our results agree with (i) and (iii), while strain-induced cracking prevents an accurate description of the effect mentioned in (ii). Further theoretical investigations should take into account not only strain [4] but also the oxygen degrees of freedom [80] in order to provide a more accurate description of the O2p and V3d orbitals overlap, most relevant for describing the conductivity in the  $ab_R$ -plane, and of the cracking along  $c_R$ . Such estimates would be adequate for a quantitative, rather than merely qualitative, comparison with our experimental data.

## 5. Conclusion

In summary, we observed a large anisotropy in the properties of highly strained VO<sub>2</sub> thin films, using THz-TDS. The increased value of the MIT temperature along  $c_R$  ( $T_{MI}^{cR}$ ) compared to the structural transition temperature ( $T_{St}$ ) is a clear signature of a Mott- rather than Peierls-driven MIT along  $c_R$ . An  $e_g^\pi$  orbital tuning picture is proposed to explain the reduced value of the high-temperature conductivity along  $b_R$ ,  $\sigma_{bR}$ , although a crack-induced conductivity decrease cannot be conclusively ruled out. Additional experiments are needed to clarify the mechanism of the MIT in strained VO<sub>2</sub>, mainly in the direction perpendicular to  $c_R$ . This would allow development of a more comprehensive phase diagram for this material. In general, epitaxial strain engineering is a powerful tool that has the potential to enable a careful tuning of the MIT in numerous other correlated electron materials, thereby providing a viable route towards technologically relevant multifunctionality and increased understanding of the microscopic origin of the MIT.

## Acknowledgments

We thank Kebin Fan and Wei Zhang for SEM sample characterization. We acknowledge support from DOE—Basic Energy Sciences under grant no. DE-FG02-09ER46643 (EA, ML and RDA). EA acknowledges support from Fundação para a Ciência e a Tecnologia, Portugal, through a doctoral degree fellowship (SFRH/BD/47847/2008).

## References

- [1] Ladd L A and Paul W 1969 Optical and transport properties of high quality crystals of  $V_2O_4$  near the metallic transition temperature *Solid State Commun.* **7** 425–8
- [2] Andersson G 1956 Studies on vanadium oxides II. The crystal structure of vanadium dioxide *Acta Chem. Scand.* **10** 623–8
- [3] Biermann S, Poteryaev A, Lichtenstein A and Georges A 2005 Dynamical singlets and correlation-assisted Peierls transition in  $VO_2$  *Phys. Rev. Lett.* **94** 026404
- [4] Lazarovits B, Kim K, Haule K and Kotliar G 2010 Effects of strain on the electronic structure of  $VO_2$  *Phys. Rev. B* **81** 115117
- [5] Kim H-T, Lee Y W, Kim B-J, Chae B-G, Yun S J, Kang K-Y, Han K-J, Yee K-J and Lim Y-S 2006 Monoclinic and correlated metal phase in  $VO_2$  as evidence of the Mott transition: coherent phonon analysis *Phys. Rev. Lett.* **97** 266401
- [6] Qazilbash M, Tripathi A, Schafgans A, Kim B-J, Kim H-T, Cai Z, Holt M, Maser J, Keilmann F, Shpyrko O and Basov D 2011 Nanoscale imaging of the electronic and structural transitions in vanadium dioxide *Phys. Rev. B* **83** 165108
- [7] Arcangeletti E, Baldassarre L, Di Castro D, Lupi S, Malavasi L, Marini C, Perucchi A and Postorino P 2007 Evidence of a pressure-induced metallization process in monoclinic  $VO_2$  *Phys. Rev. Lett.* **98** 196406
- [8] Kim H-T, Chae B-G, Youn D-H, Kim G, Kang K-Y, Lee S-J, Kim K and Lim Y-S 2005 Raman study of electric-field-induced first-order metal–insulator transition in  $VO_2$ -based devices *Appl. Phys. Lett.* **86** 242101
- [9] Driscoll T, Kim H-T, Chae B-G, Kim B-J, Lee Y-W, Marie N, Jokerst Palit S, Smith D R, Di Ventra M and Basov D N 2009 Memory metamaterials *Science* **325** 1518–21
- [10] Hilton D, Prasankumar R, Fourmaux S, Cavalleri A, Brassard D, El Khakani M, Kieffer J, Taylor A and Averitt R 2007 Enhanced photosusceptibility near  $T_c$  for the light-induced insulator-to-metal phase transition in vanadium dioxide *Phys. Rev. Lett.* **99** 226401
- [11] Muraoka Y, Ueda Y and Hiroi Z 2002 Large modification of the metal–insulator transition temperature in strained  $VO_2$  films grown on  $TiO_2$  substrates *J. Phys. Chem. Solids* **63** 965–7
- [12] Lu J K, West G and Wolf S A 2008 Very large anisotropy in the dc conductivity of epitaxial  $VO_2$  thin films grown on (011) rutile  $TiO_2$  substrates *Appl. Phys. Lett.* **93** 262107
- [13] Zhang S, Yen Chou J and Lincoln Lauhon J 2009 Direct correlation of structural domain formation with the metal insulator transition in a  $VO_2$  nanobeam *Nano Lett.* **9** 4527–32
- [14] Jepsen P U, Bernd Fischer M, Thoman A, Helm H, Suh J Y, Lopez R and Haglund R F Jr 2006 Metal–insulator phase transition in a  $VO_2$  thin film observed with terahertz spectroscopy *Phys. Rev. B* **74** 205103
- [15] Nakajima M, Takubo N, Hiroi Z, Ueda Y and Suemoto T 2008 Photoinduced metallic state in  $VO_2$  proved by the terahertz pump–probe spectroscopy *Appl. Phys. Lett.* **92** 011907
- [16] Cocker T L, Titova L V, Fourmaux S, Bandulet H C, Brassard D, Kieffer J C, El Khakani M A and Hegmann F A 2010 Terahertz conductivity of the metal–insulator transition in a nanogranular  $VO_2$  film *Appl. Phys. Lett.* **97** 221905
- [17] Chen C, Zhu Y, Zhao Y, Lee J H, Wang H, Bernussi A, Holtz M and Fan Z 2010  $VO_2$  multidomain heteroepitaxial growth and terahertz transmission modulation *Appl. Phys. Lett.* **97** 211905
- [18] Choi S B *et al* 2011 Nanopattern enabled terahertz all-optical switching on vanadium dioxide thin film nanopattern enabled terahertz all-optical switching on vanadium *Appl. Phys. Lett.* **98** 071105
- [19] Goldflam M D *et al* 2011 Reconfigurable gradient index using  $VO_2$  memory metamaterials *Appl. Phys. Lett.* **99** 044103
- [20] Mandal P, Speck A, Ko C and Ramanathan S 2011 Terahertz spectroscopy studies on epitaxial vanadium dioxide thin films across the metal–insulator transition *Opt. Lett.* **36** 1927–9
- [21] Pashkin A, Kubler C, Ehrke H, Lopez R, Halabica A, Haglund R F Jr, Huber R and Leitenstorfer A 2011 Ultrafast insulator–metal phase transition in  $VO_2$  studied by multiterahertz spectroscopy *Phys. Rev. B* **19** 195120

- [22] Zhao Y, Lee J H, Zhu Y, Nazari M, Chen C, Wang H, Bernussi A, Holtz M and Fan Z 2012 Structural, electrical and terahertz transmission properties of VO<sub>2</sub> thin films grown on *c*-, *r*- and *m*-plane sapphire substrates *J. Appl. Phys.* **111** 053533
- [23] West G K, Lu J, Yu J, Kirkwood D, Chen W, Pei Y, Claassen J and Wolf S A 2008 Growth and characterization of vanadium dioxide thin films prepared by reactive-biased target ion beam deposition *J. Vac. Sci. Technol. A* **26** 133–9
- [24] Jepsen P U, Cooke D G and Koch M 2011 Terahertz spectroscopy and imaging—modern techniques and applications *Laser Photonics Rev.* **5** 124–66
- [25] McWhan D B, Marezio M, Remeika J P and Dernier P D 1974 X-ray diffraction study of metallic VO<sub>2</sub> *Phys. Rev. B* **10** 490–5
- [26] Cao J, Ertekin E, Srinivasan V, Fan W, Huang S, Zheng H, Yim J W L, Khanal D R, Ogletree D F, Grossman J C and Wu J 2009 Strain engineering and one-dimensional organization of metal insulator domains in single-crystal vanadium dioxide beams *Nature Nanotechnol.* **4** 732–7
- [27] Kucharczyk D and Niklewski T 1979 Accurate x-ray determination of the lattice parameters and the thermal expansion coefficients of VO<sub>2</sub> near the transition temperature *J. Appl. Crystallogr.* **12** 370–3
- [28] Wu J, Gu Q, Beth Guiton S, de Leon N P, Ouyang L and Park H 2006 Strain-induced self organization of metal–insulator domains in single-crystalline VO<sub>2</sub> nanobeams *Nano Lett.* **6** 2313–7
- [29] Sohn J I, Joo H J, Ahn D, Lee H H, Porter E A, Kim K, Kang D J and Welland M E 2009 Surface-stress-induced Mott transition and nature of associated spatial phase transition in single crystalline VO<sub>2</sub> nanowires *Nano Lett.* **9** 3392–7
- [30] Jones A C, Berweger S, Wei J, Cobden D and Raschke M B 2010 Nano-optical investigations of the metal–insulator phase behavior of individual VO<sub>2</sub> microcrystals *Nano Lett.* **10** 1574–81
- [31] Jördens C, Scheller M, Wichmann M, Mikulics M, Wiesauer K and Koch M 2009 Terahertz birefringence for orientation analysis *Appl. Opt.* **48** 2037–44
- [32] Goodenough J 1971 The two components of the crystallographic transition in VO<sub>2</sub> *J. Solid State Chem.* **3** 490–500
- [33] Eyert V 2002 The metal–insulator transitions of VO<sub>2</sub>: a band theoretical approach *Ann. Phys., Lpz.* **11** 650–702
- [34] Zylbersztein A and Mott N F 1975 Metal–insulator transition in vanadium dioxide *Phys. Rev. B* **11** 4383–95
- [35] Berglund C N and Guggenheim H J 1969 Electronic properties of VO<sub>2</sub> near the semiconductor–metal transition *Phys. Rev.* **185** 1022–33
- [36] Nagashima K, Yanagida T, Tanaka H and Kawai T 2006 Stress relaxation effect on transport properties of strained vanadium dioxide epitaxial thin films *Phys. Rev. B* **74** 172106
- [37] Qazilbash M, Burch K, Whisler D, Shrekenhamer D, Chae B, Kim H and Basov D 2006 Correlated metallic state of vanadium dioxide *Phys. Rev. B* **74** 205118
- [38] Pouget J P, Launois H, D’Haenens J P, Merenda P and Rice T M 1975 Electron localization induced by uniaxial stress in pure VO<sub>2</sub> *Phys. Rev. Lett.* **35** 873–5
- [39] Goodenough J B and Hong H Y-P 1973 Structures and a two-band model for the system V<sub>1-x</sub>Cr<sub>x</sub>O<sub>2</sub> *Phys. Rev. B* **8** 1323–31
- [40] Marezio M, McWhan D B, Remeika J P and Dernier P D 1972 Structural aspects of the metal–insulator transitions in Cr-doped VO<sub>2</sub> *Phys. Rev. B* **5** 2541–51
- [41] Pouget J P and Launois H 1976 Metal–insulator phase transition in VO<sub>2</sub> *J. Phys.: Condens. Matter* **37** 49–57
- [42] Villeneuve P, Drillon G and Hagenmuller M 1973 Contribution à l’étude structurale des phases V<sub>1-x</sub>Cr<sub>x</sub>O<sub>2</sub> *Mater. Res. Bull.* **8** 1111–22
- [43] Macchesney J and Guggenheim H 1969 Growth and electrical properties of vanadium dioxide single crystals containing selected impurity ions *J. Phys. Chem. Solids* **30** 225–34
- [44] McWhan D B, Rice T M and Remeika J P 1969 Mott transition in Cr-doped V<sub>2</sub>O<sub>3</sub> *Phys. Rev. Lett.* **23** 1384–7
- [45] Neuman C H, Lawson A W and Brown R F 1964 Pressure dependence of the resistance of VO<sub>2</sub> *J. Chem. Phys.* **41** 1591–5

- [46] Berglund C N and Jayaraman A 1969 Hydrostatic-pressure dependence of the electronic properties of VO<sub>2</sub> near the semiconductor–metal transition temperature *Phys. Rev.* **185** 1034–9
- [47] Sepúlveda N, Rúa A, Cabrera R and Fernández F 2008 Young modulus of VO<sub>2</sub> thin films as a function of temperature including insulator-to-metal transition regime *Appl. Phys. Lett.* **92** 191913
- [48] Béteille F and Livage J 1998 Optical switching in VO<sub>2</sub> thin films *J. Sol–Gel Sci. Technol.* **13** 915–21
- [49] Villeneuve G, Bordet A, Casalot A, Pouget J P, Launois H and Lederer P 1972 Contribution to the study of the metal–insulator transition in the V<sub>1-x</sub>Nb<sub>x</sub>O<sub>2</sub> system I. Crystallographic and transport properties *J. Phys. Chem. Solids* **33** 1953–9
- [50] Piccirillo C, Binions R and Parkin I P 2007 Nb-doped VO<sub>2</sub> thin films prepared by aerosol-assisted chemical vapour deposition *Eur. J. Inorg. Chem.* **2007** 4050–5
- [51] Hörlin M, Niklewski T and Nygren T 1973 Magnetic, electrical and thermal studies on the V<sub>1-x</sub>Mo<sub>x</sub>O<sub>2</sub> system with  $0 < x < 0.20$  *Mater. Res. Bull.* **8** 179–90
- [52] Holman K, McQueen T, Williams A, Klimczuk T, Stephens P, Zandbergen H, Xu Q, Ronning F and Cava R 2009 Insulator to correlated metal transition in V<sub>1-x</sub>Mo<sub>x</sub>O<sub>2</sub> *Phys. Rev. B* **79** 245114
- [53] Nygren M and Israelsson M 1969 A DTA study of the semiconductor–metallic transition temperature in V<sub>1-x</sub>W<sub>x</sub>O<sub>2</sub>,  $0 < x < 0.067$  *Mater. Res. Bull.* **4** 881–6
- [54] Chae B G, Kim H T and Yun S J 2008 Characteristics of W- and Ti-doped VO<sub>2</sub> thin films prepared by sol–gel method *Electrochem. Solid-State Lett.* **11** D53–5
- [55] Sävborgae Ö and Nygren M 1977 Magnetic, electrical and thermal studies of the V<sub>1-x</sub>Re<sub>x</sub>O<sub>2</sub> system with  $0 < x < 0.15$  *Phys. Status Solidi a* **43** 645–52
- [56] Bayard M 1975 Propriétés magnétiques et électriques de l’oxyfluorure de formule VO<sub>2-x</sub>F<sub>x</sub> *J. Solid State Chem.* **12** 41–50
- [57] Kristensen I K 1968 Semiconductor-to-semiconductor transition in the pseudobinary system TiO<sub>2</sub>–VO<sub>2</sub> *J. Appl. Phys.* **39** 5341–2
- [58] Marinder B-O and Magnéli A 1957 Metal–metal bonding in some transition metal oxides *Acta Chem. Scand.* **11** 1635–40
- [59] Gu Q, Falk A, Wu J, Ouyang L and Park H 2007 Current-driven phase oscillation and domain-wall propagation in W<sub>x</sub>V<sub>1-x</sub>O<sub>2</sub> nanobeams *Nano Lett.* **7** 363–6
- [60] Drillon M and Villeneuve G 1974 Diagramme de phases du système V<sub>1-x</sub>Al<sub>x</sub>O<sub>2</sub> *Mater. Res. Bull.* **9** 1199–208
- [61] Kosuge K 1967 The phase transition in VO<sub>2</sub> *J. Phys. Soc. Japan* **22** 551–7
- [62] Pollert E, Villeneuve G, Ménil F and Hagenmuller P 1976 Le système V<sub>1-x</sub>Fe<sub>x</sub>O<sub>2</sub>: propriétés structurales et magnétiques *Mater. Res. Bull.* **11** 159–66
- [63] Pintchovski F, Glaunsinger W S and Navrotsky A 1978 Experimental study of the electronic and lattice contributions to the VO<sub>2</sub> transition *J. Phys. Chem. Solids* **39** 941–9
- [64] Kitahiro I and Watanabe A 1967 Shift of transition temperature of vanadium dioxide crystals *Japan. J. Appl. Phys.* **6** 1023–4
- [65] Lee M-H, Kim M-G and Song H-K 1996 Thermochromism of rapid thermal annealed VO<sub>2</sub> and Sn-doped VO<sub>2</sub> thin films *Thin Solid Films* **290–291** 30–3
- [66] Everhart J B and MacChesney C R 1968 Anisotropy in the electrical resistivity of vanadium dioxide single crystals *J. Appl. Phys.* **39** 2872–4
- [67] Barker H J, Verleur A S and Guggenheim H W 1966 Infrared optical properties of vanadium dioxide above and below the transition temperature *Phys. Rev. Lett.* **17** 1286–9
- [68] Bongers P F 1965 Anisotropy of the electrical conductivity of VO<sub>2</sub> single crystals *Solid State Commun.* **3** 275–7
- [69] Verleur W H, Barker A S and Berglund C N 1968 Optical properties of VO<sub>2</sub> between 0.25 and 5 eV *Phys. Rev.* **172** 788–98
- [70] Continenza A, Massidda S and Posternak M 1999 Self-energy corrections in VO<sub>2</sub> within a model GW scheme *Phys. Rev. B* **60** 15699–704
- [71] Mossanek R J O and Abbate M 2007 Optical response of metallic and insulating VO<sub>2</sub> calculated with the LDA approach *J. Phys.: Condens. Matter* **19** 346225

- [72] Lysenko S, Vikhnin V, Fernandez F, Rua A and Liu H 2007 Photoinduced insulator-to-metal phase transition in VO<sub>2</sub> crystalline films and model of dielectric susceptibility *Phys. Rev. B* **75** 075109
- [73] Tomczak J and Biermann S 2009 Optical properties of correlated materials: generalized Peierls approach and its application to VO<sub>2</sub> *Phys. Rev. B* **80** 085117
- [74] Minomura S and Hagasaki H 1964 The effect of pressure on the metal-to-insulator transition in V<sub>2</sub>O<sub>4</sub> and V<sub>2</sub>O<sub>3</sub> *J. Phys. Soc. Japan* **19** 131–2
- [75] Gregg J M and Bowman R M 1997 The effect of applied strain on the resistance of VO<sub>2</sub> thin films *Appl. Phys. Lett.* **71** 3649–51
- [76] Sakai J 2008 Electrical measurements of a VO<sub>2</sub> thin film under high pressure of 25 GPa generated by a load-controllable point-contact structure *J. Appl. Phys.* **104** 073703
- [77] Wentzcovitch M R, Schulz W and Allen B P 1994 VO<sub>2</sub>: Peierls or Mott–Hubbard? A view from band theory *Phys. Rev. Lett.* **72** 3389–92
- [78] Tanaka A 2003 A new scenario on the metal–insulator transition in VO<sub>2</sub> *J. Phys. Soc. Japan* **72** 2433–6
- [79] Liebsch A, Ishida H and Bihlmayer G 2005 Coulomb correlations and orbital polarization in the metal–insulator transition of VO<sub>2</sub> *Phys. Rev. B* **71** 085109
- [80] Laverock J *et al* 2012 Strain dependence of bonding and hybridization across the metal–insulator transition of VO<sub>2</sub> *Phys. Rev. B* **85** 081104
- [81] Koide S and Takei H 1967 Epitaxial growth of VO<sub>2</sub> single crystals and their anisotropic properties in electrical resistivities *J. Phys. Soc. Japan* **22** 946–7